Using an impact hammer to estimate elastic modulus and thickness of a sample during an osteotomy

Alexis Hubert, Giuseppe Rosi, Romain Bosc, Guillaume Haïat

Using an impact hammer to estimate elastic modulus and thickness of a sample during an osteotomy

Alexis Hubert[a], Giuseppe Rosi[a], Romain Bosc[b,c], Guillaume Haiat[a]

[a] CNRS, Laboratoire de Modélisation et de Simulation Multi-Echelle,
UMR CNRS 8208,61 Avenue du Général de Gaulle, Créteil 94010, France
[b] INSERM U955, Team 16, Créteil, France; Vaccine Research Institute (VRI), Faculté de Médecine, Créteil, France; Université Paris Est, Créteil, France
[c] Hopital Henri Mondor, Plastic, Reconstructive, Aesthetic and Maxillofacial Surgery Department, 50, avenue du Maréchal de Lattre de Tassigny, 94000 Créteil, France

Corresponding author:
Guillaume HAÏAT
Laboratoire de Modélisation et de Simulation Multi Echelle, UMR CNRS 8208,
61 avenue du Général de Gaulle,
94010 Créteil, France
tel : (33) 1 45 17 14 41
fax : (33) 1 45 17 14 33
e-mail : guillaume.haiat@univ-paris-est.fr

Submitted to J Biomech Eng

Abstract

Performing an osteotomy with a surgical mallet and an osteotome is a delicate intervention mostly based on the surgeon proprioception. It remains difficult to assess the properties of bone tissue being osteotomized. Mispositioning of the osteotome or too strong impacts may lead to bone fractures which may have dramatic consequences. The objective of this study is to determine whether an instrumented hammer may be used to retrieve information on the material properties around the osteotome tip. A hammer equipped with a piezoelectric force sensor was used to impact 100 samples of different composite materials and thicknesses. A model-based inversion technique was developed based on the analysis of two indicators derived from the analysis of the variation of the force as a function of time in order to i) classify the samples depending on their material types, ii) determine the materials stiffness and iii) estimate the samples thicknesses. The model resulting from the classification using Support Vector Machines (SVM) learning techniques can efficiently predict the material of a new sample, with an estimated 89% prediction performance. A good agreement between the forward analytical model and the experimental data was obtained, leading to an average error lower than 10% in the samples thickness estimation. Based on these results, navigation and decision-support tools could be developed and allows surgeons to adapt their surgical strategy in a patient-specific manner.

Keywords: Osteotomy; impact hammer; surgical technique; impact; vibration analysis

1. Introduction

An osteotome is a surgical tool comparable to a bone chisel with a wedge shaped cutting edge. Osteotomes are used to cut and/or shape bone and cartilage tissues in order to modify their geometry. The use of osteotomes has been reported in various surgical fields. In maxillo-facial surgery, osteotomes are used to cut the maxilla bone or split and expand the bone ridge or compress trabecular bone tissue to obtain a better bone density and primary stability of dental implants [1, 2]. In orthopedic surgery, osteotomies are realized to cut bone tissue and to shave off osteoperiosteal grafts, as well as to remove the cartilage and subchondral bone [3]. The osteotome is a standard instrument in plastic surgery too [4], especially in genioplasty or rhinoplasty, since it is used to correct nasal deviation due to bony deformation, to narrow the bony nasal vault, or to reduce the dorsal hump [5, 6].

Despite their routine clinical use, there remain risks of surgical failure associated with osteotomies. One of the main difficulties lies in that visual control of the tissue being osteotomized is not always possible. Image-guided surgery is used in several surgical fields to assist and guide the surgeon using preoperative and/or real-time intraoperative images. Various tools have been developed in recent years, like intraoperative navigated ultrasound, dedicated moveable intraoperative computed tomography (CT) units, or intraoperative magnetic resonance imaging [7, 8]. However, such procedures are complex, sometimes radiating and may increase the surgery duration, which makes them ill-adapted to provide assistance during osteotomies. Therefore, they are not used routinely in many cases and most surgeons still rely on their proprioception. Biomechanical approaches may be more appropriate than other imaging techniques in order to provide information on the biomechanical properties of the tissue located around the osteotome, which may in turn guide the surgeon in the realization of the following impacts, in particular in terms of energy.

Biomechanical methods may be used to assess bone thickness around the osteotome tip, which could help the surgeon follow the progression of the osteotome and adapt the surgical strategy. In particular, in the case of rhinoplasty, the nasal bones are thicker where they connect to frontal bones, and thinner in their inferior lateral part where they articulate with the maxilla and the upper lateral cartilage [9]. A low osteotomy may cause nasal obstruction if the fragment is displaced medially into the airway. A high osteotomy may become palpable and visible under the skin if placed above the thick nasofacial sulcus [9, 10]. Information on the bone thickness at the osteotome tip could be used to check the correct placement of the osteotomy and follow the osteotome path. The determination of the mechanical properties of bone tissues being osteotomized could also be helpful to assess the correct propagation of the crack at the osteotome tip, and to evaluate whether the osteotomy is complete. In rhinoplasty, an incomplete osteotomy may result in a difficult displacement of the nasal bones and may cause deviation of the bony vault [10]. On the contrary, incomplete fractures are sometimes preferable in older patients to avoid comminution of the bony fragment [9]. Another example where complete fracture is not desired is to preserve the attachments between the nasal bones and upper lateral cartilages. An uncontrolled crack propagation may be associated to nasal vault collapse when these attachments become disrupted, leading to an inverted V deformity [5, 11, 9]. The surgeon has little sense of the mechanical properties of the bone tissue being osteotomized, thus making the apparition of adverse cracks, fractures or disruptions difficult to detect. A long learning curve is necessary for surgeons to master the optimal energy and the number of successive impacts required to avoid such events, and information on the bone tissue condition at the osteotome tip could help determining the moment when impacting bone tissue should be stopped.

Interestingly, our group has developed a method based on impact analyses in order to assess implant stability. The method uses a hammer equipped with a piezoelectric force sensor to measure the time variation of the force applied to the ancillary during the insertion of acetabular cup (AC) and femoral stem implants. Previous studies showed that impact analysis could be used to assess the primary stability of such implants. Different indicators based on the hammer-ancillary contact duration [12, 13] and on the impact momentum [14] were tested *in vitro*, then *ex vivo* [15]. To improve the understanding of mechanical phenomena occurring during the AC insertion, static [16] and dynamic [17] finite element models were developed. Eventually, pre-clinical cadaveric studies are being carried out to test the device in situations closed to those met in the operating room [18, 19].

The long-term objectives of the method described below are (1) to detect a change of material during an osteotomy, and to attribute a material type (for example cartilage, trabecular or cortical bone) to each material met by the osteotome tip, (2) to determine the stiffness of bone tissue around the tip of the osteotome and (3) to estimate the thickness of the materials being dissected. These three pieces of information may be used to assist surgeons during osteotomy via a decision support system. The present study considers various materials including bone-mimicking materials, but no cartilage nor bone tissues, because the aim was to show the feasibility of using an impact hammer to characterize the material geometrical and material properties, and establishing the proof of concept on non-biological material is an ethical requirement before considering actual configurations met in the operating room. The aim of the present study was to investigate whether a technique based on impact analysis can be applied to retrieve information on the geometrical and mechanical properties of the material located at the tip of an osteotome, which will be done using an in vitro model. The time variation of the force applied to the osteotome during impacts produced with an instrumented mallet was analyzed in order to retrieve information on the stiffness and thickness of the material being osteotomized.

2. Material and methods

2.1. Experimental measurements

A schematic representation of the experimental set-up is shown in Fig 1. A 260 g surgical mallet (32-6906-26, Zepf, Tuttlingen, Germany) was used in this study to produce impacts on an osteotome (32-6002-10, Zepf, Tuttlingen, Germany) having a 10 mm long cutting edge. The hammer and the osteotome are used in clinical practice to realize osteotomies. For each impact, the osteotome was held manually, similarly to what is done in the clinic. A dynamic piezoelectric force sensor (208C04, PCB Piezotronics, Depew, NY, USA) with a measurement range up to 4.45 kN in compression was screwed in the center of the impacting face of the hammer to measure the force applied to the osteotome. A data acquisition module (NI 9234, National Instruments, Austin, TX, USA) with a sampling frequency of 51.2 kHz and a resolution of 24 bits was used to record the time variation of the force exerted on the osteotome. The data were transferred to a computer and recorded using a Labview interface (National Instruments, Austin, TX, USA) for a duration of 2 ms.

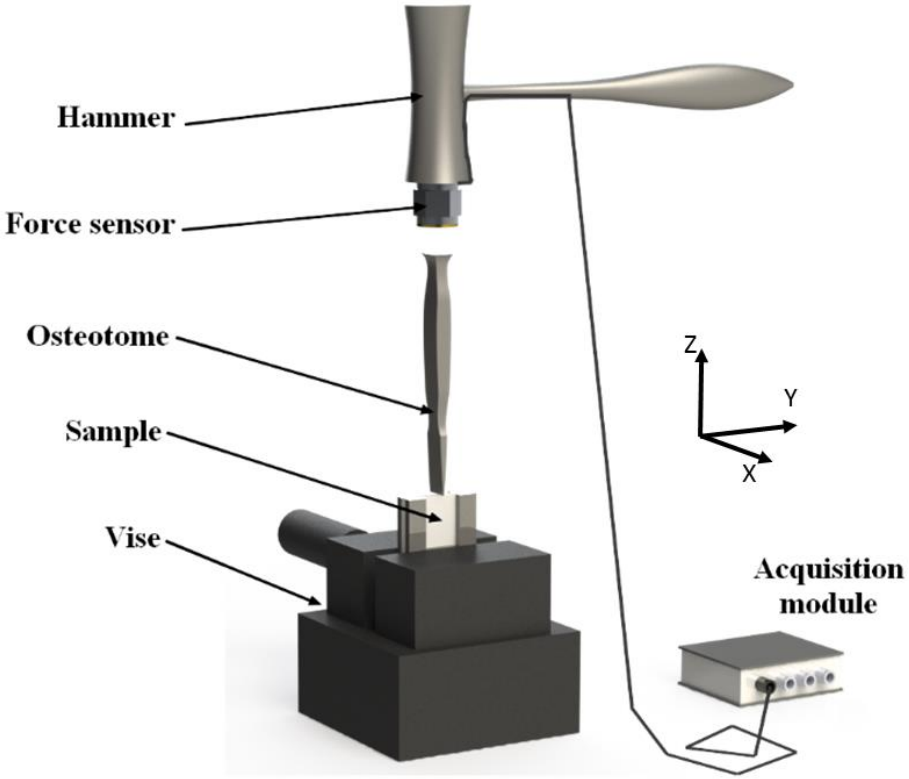

Figure 1 - Schematic representation of the experimental set-up used for impaction of the osteotome on the samples. The sample is in the plane (*YZ)* and the plane of the osteotome is in the plane *(XZ)*.

The osteotome was inserted into samples constituted by plates made of the following materials: three-plies ordinary birch plywood, polycarbonate (Nudec, Barcelona, Spain), polyurethane resin (SmoothCast 300, Smooth-On, Easton, PA, USA) and orthobone (commercial bone mimicking phantom) of three different densities (3B Scientific, Hamburg, Germany). The Young's modulus of each material was measured with classical tensile tests. To do so, the samples were tested using a mechanical testing machine (DY25, Adamel Lhomargy, Roissy en Brie, France) and the Young's modulus of each material was derived from the slope of the variation of the force as a function of the deformation taking into account the sample geometry. The experiment was reproduced 5 times for each material using different sample and the reproducibility of the measurement was of the order of 10% for all samples. It was difficult to measure with accuracy the mechanical loss using tensile test using our testing device, which was therefore taken from the literature [20, 21, 22, 23, 24] (see Table 1). The following notation will be used for each material: plywood (PW), polycarbonate (PC), resin (RS), orthobone 10 PCF (O1), orthobone 20 PCF (O2), orthobone 30 PCF (O3). The dimensions of all plates were 3 × 4.5 cm. The thickness of each plate was measured using a caliper, and the values ranged from 2 to 8 mm. Table 1 also indicates the average, standard deviation, minimum and maximum values of the samples thickness distribution, as well as the number of samples for each material. A total number of 100 samples was considered in this study. The following notation will be used for each material: plywood (PW), polycarbonate (PC), resin (RS), orthobone 10 PCF (O1), orthobone 20 PCF (O2), orthobone 30 PCF (O3).

Material	E (MPa)	tanδ	d_m (mm)	σ_d (mm)	d^- (mm)	d^+ (mm)	N
Plywood	2400	0.01	4.7	1.5	3.0	6.0	11
Polycarbonate	1300	0.02	4.9	1.2	3.0	6.0	20
Resin	500	0.03	4.7	1.5	2.4	6.8	17
Orthobone 10 PCF	41	0.03	4.4	1.4	2.4	7.1	18
Orthobone 20 PCF	250	0.03	4.1	1.5	2.5	7.1	15
Orthobone 30 PCF	380	0.03	4.5	1.2	2.1	5.8	19

Table 1: Mechanical properties of the six material types, and corresponding plates thickness distribution. E denotes the Young's modulus, tanδ the mechanical loss, d_m the mean plate thickness, σ_d the standard deviation of the plate thickness, d^- the minimum plate thickness, d^+ the maximum plate thickness, and N the number of samples of each material. The reproducibility of the measurement of E is equal to around 10% for all samples.

For each impact, the time dependence of the force applied to the osteotome was measured using the device described above, leading to a radiofrequency signal denoted $s(t)$. An example of typical signal obtained with a 3 mm thick plywood sample is shown in Fig. 2. A dedicated signal processing technique was applied to $s(t)$ using information derived from the different peaks obtained in the signal. For the first two peaks of $s(t)$, the maximum peak amplitude a_p, the time of its center t_p, and the root mean square width w_p were determined by fitting a Gaussian function with a time windows centered on t_p and corresponding to the time when $s(t) > a_p/5$. A first indicator τ corresponding to the difference between the times of the second and first peaks of $s(t)$ was determined. τ is referred to as the *second peak time* in what follows. A second indicator λ was defined as the ratio of the second peak integral I_2 on the first peak integral I_1, and was calculated using the Gaussian integral $I = (2\pi)^{0.5} \times w_p \times a_p$ as an approximation of the peak integral. The integral of the force over a time interval is called the impulse, and corresponds to the change of momentum during this interval. $\lambda = I_2/I_1$ is referred to as the *impulse ratio* in what follows.

Each plate sample was clamped between two jaws in a vise and the tip of the osteotome was brought to a depth of 2 mm into the material before the test and we verified that no visible variation of this depth was obtained after 30 impacts. The plane of the osteotome (XZ) was perpendicular to that of the plate (YZ). The osteotome was impacted around 30 times with a maximum force comprised between 150 and 250 N, which corresponds to a low energy impact that is not likely to induce crack propagation in each material. The values of the indicators τ and λ were determined for the thirty impacts and averaged to derive mean values of τ and λ for each sample.

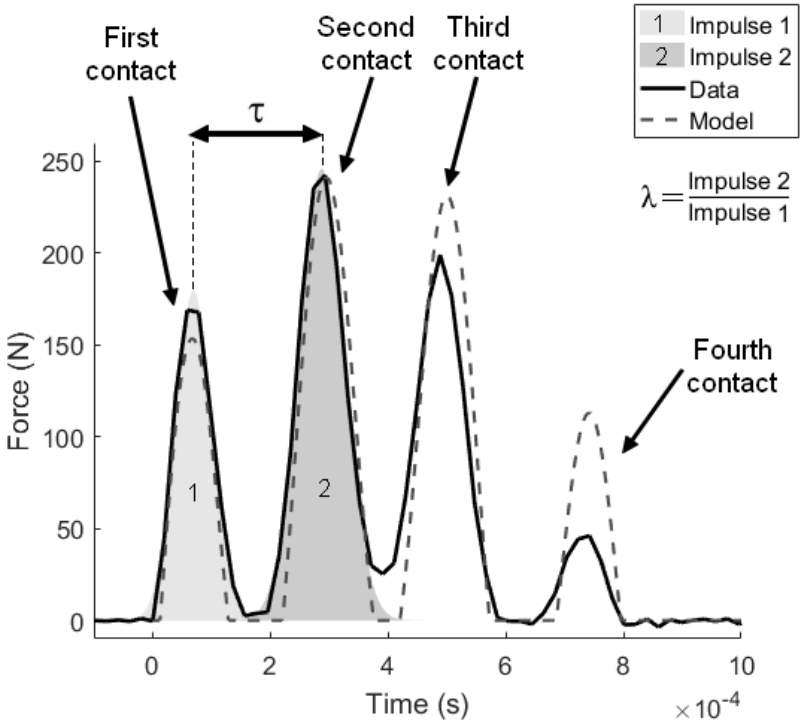

Figure 2 – Signals corresponding to the variation of the force applied to the osteotome as a function of time obtained experimentally (solid line) and analytically (dashed line) for an impact realized on a 3 mm thick plywood sample. The first (respectively second and third) contact correspond to the first (respectively second and third) peak. The analytical signal corresponds to the solution given by Eqs. 1-2 ($m_h\ddot{x}_B$ is plotted) by considering: v_h= 0.1 m/s, E = 2400 MPa and tan δ = 0.01. The experimental signal correspond to one given impact and was not averaged.

2.2. Modeling

A simple 1-D mechanical model described schematically in Fig. 3 (a) was developed to predict the response of the plate-osteotome system when impacted by the hammer. The osteotome was modeled by an elastic spring of mass m_o and stiffness k_o. The plate was modeled as a viscoelastic material using the Kelvin-Voigt model [25, 21] with a stiffness given by $k_s = d \,.\, w \,.\, E / l$, which corresponds to the stiffness of an isotropic plate of finite thickness deformed in a direction parallel to its plane. d, w, l are the thickness (along axis X), width (along axis Y) and length (along axis Z) of the sample respectively, and E is the Young's modulus of the plate material. The viscosity η_s is given by $\eta_s = k_s \tan\delta/\omega_o$, [25, 21] where $\tan\delta$ the mechanical loss and $\omega_o = (k_s/m_o)^{0.5}$ is the pulsation. The two free parameters of the model are the thickness d and elastic modulus E of the sample. The parameter $\tan\delta$ corresponding to the viscoelastic damping was taken constant and equal to the values shown in Table 1, an assumption that will be discussed in section 4.2.2. The other parameters of the model are indicated in Table 2.

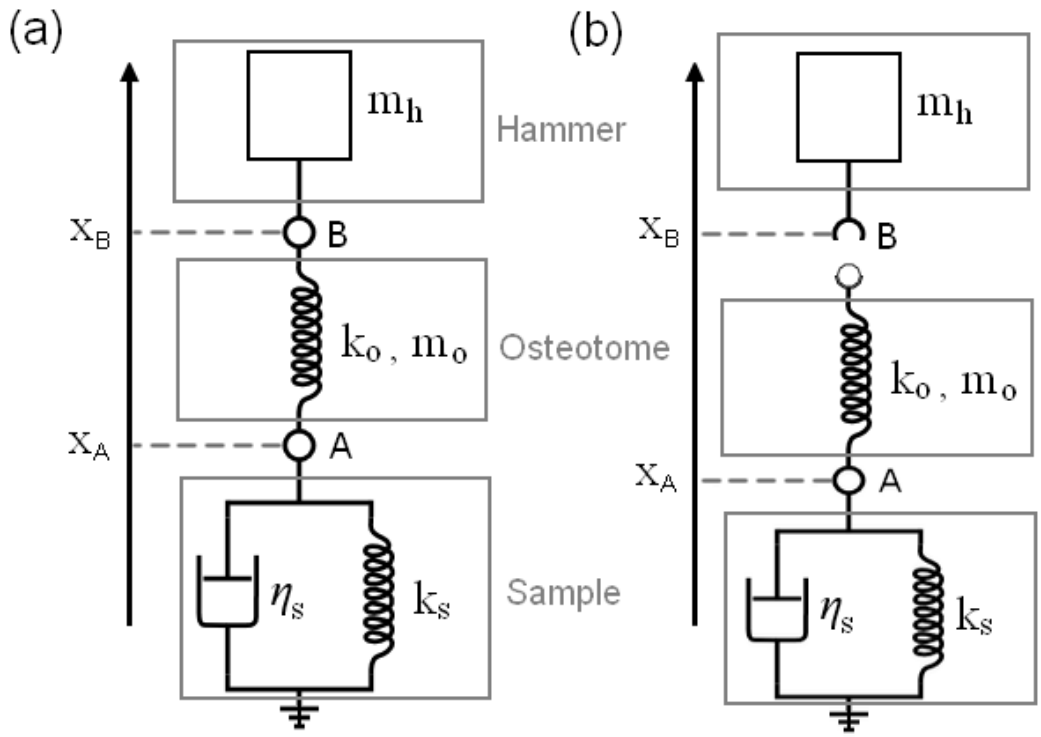

Figure 3 – Schematic representation of the acoustical model used to account for the behavior of the damped oscillating system. A is the bilateral contact point between the osteotome and the sample. B is the unilateral contact point between the osteotome and the hammer. (a): Configuration where the hammer is in contact with the osteotome. (b): Configuration where the hammer is not in contact with the osteotome. The varying parameters of the model are k_s and η_s, which correspond to the stiffness and of the viscosity of the tested samples and which are function of the sample material.

Let x_A be the position of the osteotome-sample contact point *A*, and x_B the position of the hammer-osteotome contact point. When the hammer and the osteotome are in contact, the coupled equations of motion write:

$$\begin{cases} m_o \ddot{x}_A = k_o(x_B - x_A - L_o) - k_s x_A - \eta_s \dot{x}_A \\ m_h \ddot{x}_B = -k_o(x_B - x_A - L_o) \end{cases} \quad (1)$$

When $x_B - x_A > L_o$ no contact between the osteotome and the hammer occurs in *B* (see Fig. 3(b)) and the osteotome oscillates freely without interacting with the hammer. The equations of motion then become:

$$\begin{cases} m_o \ddot{x}_A = -k_s x_A - \eta_s \dot{x}_A \\ m_h \ddot{x}_B = 0 \end{cases} \quad (2)$$

The coupled equations 1 and 2 were solved numerically using Runge-Kutta 4 formulae [26, 27, 28] implemented in the software Matlab (The Mathworks, Natick, MA, USA).

Component	Parameter	Value
Hammer	Mass m_h	260 g
	Initial velocity v_h	0.1 m/s
Osteotome	Mass m_o	52 g
	Length L_o	13.5 cm
	Stiffness k_o	$3.7 \cdot 10^7$ N/m
Sample	Length l	4.5 cm
	Width w	3 cm

Table 2: Parameters used in the acoustical model described in Fig. 3.

2.3. Data analyses

Three methods were developed to analyze the experimental data and are described below. The aim of the first method is to classify the different materials based on τ and λ. The second method provides an estimation of the materials stiffness using d and the data obtained with all samples of the same material. Conversely, the third method provides an estimation of d when the material and its mechanical properties are known.

2.3.1 Material Classification

A one-way analysis of variance (ANOVA) and Tukey-Kramer tests were performed on the parameters τ and λ to evaluate the effect of the material type on these two indicators. Statistical differences were defined at a 95% confidence level. The two indicators τ and λ were then used to perform a statistical classification. The goal of the classification was to provide a model able to predict the material of a given plate sample (among the six types considered in this study) based on the values of the two indicators τ and λ. The six material types are referred to as classes in what follows.

Support Vector Machines (SVM) learning techniques were applied to our dataset. SVM [29, 30] consist in computing hyperplanes separating the data into their respective classes. The separating hyperplanes are optimized to obtain the maximum margin between the boundary and the closest points of opposite classes – the so-called Support Vectors – on either side of the boundary.

Considering the two dimensional space (τ, λ), each plate sample #i is characterized by an averaged pair of coordinates (τ_i, λ_i) derived from the 30 impacts. SVM compute hyperplanes separating the space into regions of interest corresponding to the different material classes. Since SVM were originally designed for binary

classification, we used a multiclass, error-correcting output codes (ECOC) model [31] to take into account all six materials. The optimization was run using Matlab (The Mathworks, Natick, MA, USA).

A 5-folds cross-validation was performed to estimate the accuracy of the model. The data were partitioned into five disjoint folds of 20 samples chosen randomly. Four folds were used iteratively as training data to determine the boundaries while the last fold was retained as the validation data. The model was tested on the validation data to estimate the prediction performances of the algorithm.

2.3.2 Identification of the Young's modulus

In this subsection, an algorithm aiming at estimating the apparent Young's modulus E is presented. For each material, the algorithm takes as input data the values of τ obtained for all samples of the considered material. A model-based inversion using the forward model described in subsection 2.2 was developed to identify the optimal value of E minimizing the cost-function φ defined below. Here, the thickness d of each sample is supposed to be known. For a given set of parameter (d,E), the coupled differential equations 1 and 2 of the forward model were solved in order to determine the time variation of the force $F_o = k_o(x_B - x_A - L_o)$ applied to the osteotome. The simulated value of the second peak time $\tilde{\tau}(d,E)$ was calculated from F_o using the signal processing technique described in subsection 2.1. As showed in Table 1, the experimental data set is composed of N plate samples for each material, with a thickness distribution noted d_i with $i \in \{1,N\}$. The cost function φ corresponding to a given modulus of elasticity E is defined as:

$$\phi(E) = \sum_{i=1}^{N} \left(\tilde{\tau}(d_i, E) - \tau_i\right)^2 \tag{3}$$

where τ_i corresponds to the experimental value of τ obtained for sample #i.

A minimization algorithm using a golden section search and parabolic interpolation [32, 33] was run in order to find the optimal value of E (denoted E_{opt}) minimizing the cost-function φ. The root-mean-squared error (RMSE) and its coefficient of variation (NRMSE) were calculated to evaluate the agreement between the experimental and simulated results following:

$$\mathrm{RMSE} = \sqrt{\frac{\phi(E_{opt})}{N}} \qquad \mathrm{NRMSE} = \frac{\mathrm{RMSE}}{\tau_m}, \tag{4}$$

where τ_m is the mean second peak time of all samples of a given material type for the experimental data. The coefficient of correlation R, which corresponds to a measure of the linear dependence between the simulated and experimental values of τ was determined following:

$$R = \frac{1}{N-1} \sum_{i=1}^{N} \left(\frac{\tilde{\tau}(d_i, E_{opt}) - \tilde{\tau}_m}{\sigma_{\tilde{\tau}}} \right) \left(\frac{\tau_i - \tau_m}{\sigma_\tau} \right) \tag{5}$$

where $\tilde{\tau}_m$ is the mean second peak time of all samples of a given material type for the simulated data, and σ_τ and $\sigma_{\tilde{\tau}}$ are the standard deviation values of the experimental and simulated second peak time.

The algorithm was applied to the six different materials to identify their respective apparent Young's modulus. The logarithm of the function corresponding to the variation of $\tilde{\tau}(d, E_{opt})$ was plotted as a function of d on a log scale for each material type.

2.3.3 Thickness estimation

For each plate sample #i, the estimated thickness was given by the thickness $\tilde{d}_i$ for which $\tilde{\tau}(\tilde{d}_i, E_{opt}) = \tau_i$. The error on the thickness estimation was given by $\varepsilon_i = \left|\tilde{d}_i - d_i\right| / d_i$, where d_i is the sample thickness determined with the caliper. The mean error ε_m, maximum error ε^+ and the standard deviation σ_ε were computed for each material.

3. Results

3.1. Temporal dependence of the force applied to the osteotome

The solid line in Fig. 2 corresponds to a typical experimental signal *s(t)* representing the variation of the force applied to the osteotome as a function of time for a given impact, realized on a 3 mm thick plywood sample. As shown in Fig. 2, the signal exhibits several oscillations and four local maxima can be observed within around 1 ms after the beginning of the impact. The dashed line shows the simulated signal obtained using the model described in subsection 2.2 with the following parameters: d = 3 mm, E = 3.4 GPa and $\tan\delta$ = 0.013 corresponding to the sample. A good qualitative agreement is obtained between the experimental and simulated signals. The second peak time τ and the impulse of the first two peaks used to calculate the impulse ratio λ are indicated in Fig. 2.

3.2. Material classification

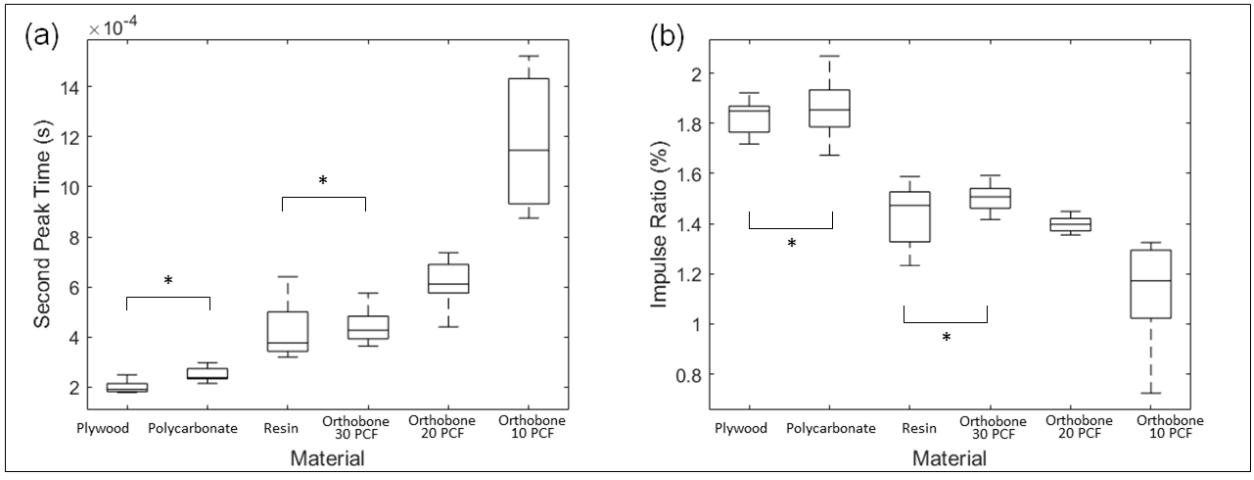

Figure 4 – Distribution of the second peak time τ (a) and the impulse ratio λ (b) obtained experimentally for the different materials. *: not statistically different.

Figure 4 shows the distribution of the two indicators τ and λ for the different material types, represented as boxplots. The central mark indicates the median and the bottom and top edges of the box indicate the lower and upper quartiles. The whiskers extend to the most extreme data points in the distribution. The data shown in Fig. 4 correspond to all thicknesses pooled, which explains the relatively important dispersion of the results.

Figure 4 shows that the material type has a significant effect on both the second peak time τ and the impulse ratio λ, which is confirmed by ANOVA since p-values for τ ($p < 10^{-42}$) and λ ($p < 10^{-35}$) are largely below the 0.05 threshold. Tukey-Kramer tests indicate that the results obtained with the different material types are significantly different from one another ($p<10^{-5}$ for all couples of materials), except for two couples of material. The indicators values obtained for PW and PC are not significantly different ($p = 0.87$ for τ and $p = 0.98$ for λ). Similarly, the indicators values obtained for O3 and RS are not significantly different ($p = 0.99$ and 0.46 for τ and λ respectively).

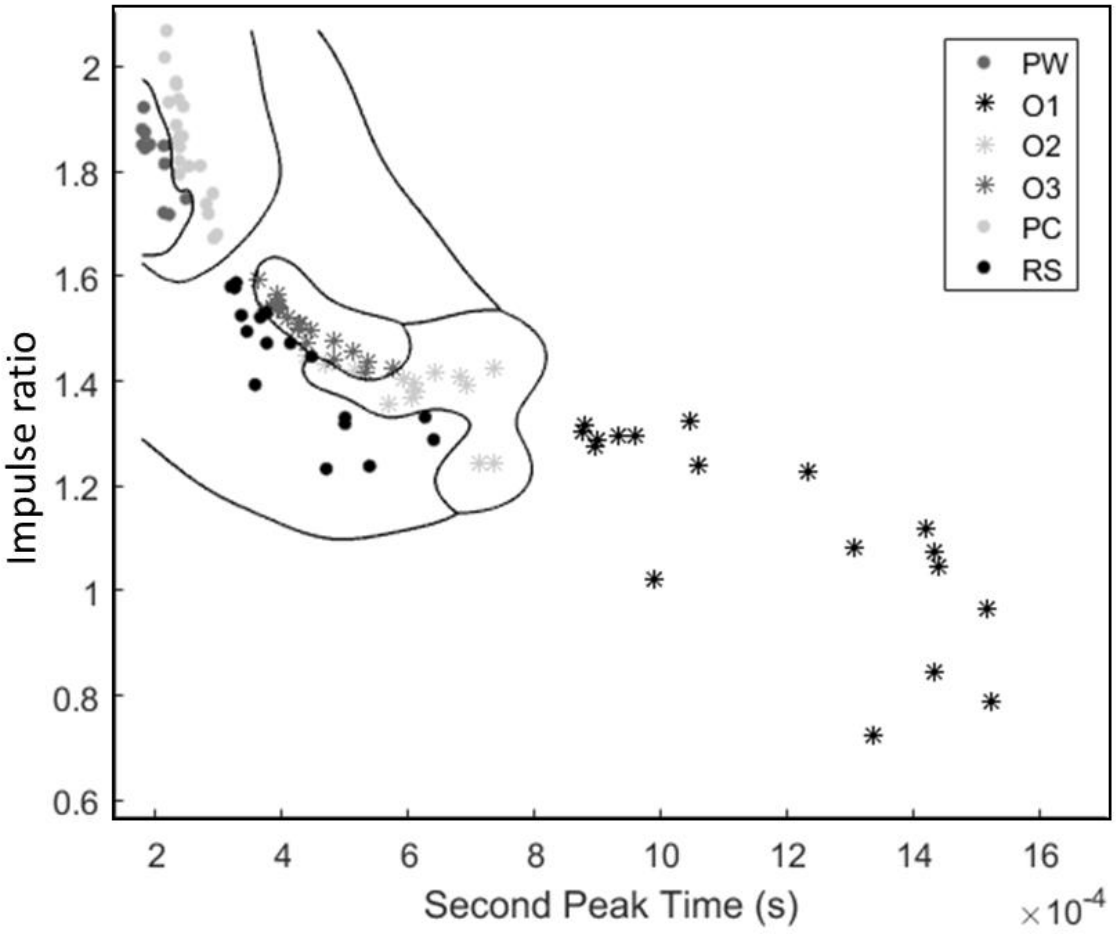

Figure 5 - Distribution of the values of τ and λ obtained for the 100 plate samples. Each material is indicated with a different marker, and the decision boundaries for material classification are indicated in solid lines.

Another representation of the distribution of both indicators is shown in Fig. 5. Regions of interests corresponding to the different materials can be distinguished, which facilitates the distinction between the material types. Each material is indicated with a different marker and the decision boundaries resulting from the trained classifier are plotted in solid lines. The cross-validation allows an estimation of the model prediction performance equal to 89%.

3.3. Identification of the Young's moduli and estimation of the sample thickness

Material	$E_{predicted}$ (MPa)	$E_{measured}$ (MPa)	RMSE ($\times 10^{-5}$ s)	NRMSE	R
PW	3400	2400	1.0	0.05	0.90
PC	1600	1300	1.1	0.04	0.94
RS	490	500	4.2	0.09	0.94
O1	60	41	10.5	0.09	0.92
O2	270	250	2.9	0.05	0.94
O3	490	380	2.2	0.05	0.94

Table 3: Predicted apparent Young's moduli ($E_{predicted}$), Young's moduli measured using the tensile tests (E) and quality assessment of the model-based inversion given by RMSE, NRMSE and R.

Table 3 shows the values of the estimated Young's moduli resulting from the model-based inversion procedure. The error on the modulus estimation compared to the tensile test value varies between 2% (for RS) and 46% (for O1). The error obtained for the estimation of E shown in Table 3 is lower than the experimental error for RS and O2. The root-mean-squared error (RMSE), coefficient of variation of the RMSE (NRMSE) and coefficient of correlation (R) are shown in Table 3 to assess the quality of the model-based inversion. Low RMSE and NRMSE and high R values indicate a good accuracy of the model. NRMSE and R are relatively independent on the magnitude of τ and can be used to compare the performance of the model for the different material types. Note that the advantage of assessing NRMSE is to lead to a value independent of τ_m, which varies significantly as a function of the material (see Fig. 4(a)).

Figure 6 shows the variation of the logarithm of the second peak time τ as a function of the thickness d on a log scale for all material tested. A good qualitative agreement is obtained between the model (solid lines) and experimental results (markers). Moreover, there were multiple samples with a single thickness only for the samples made of plywood and of polycarbonate. The results in terms of reproducibility of the measurement of are shown in Fig. 6. However, no detailed analysis was carried out because it was not the aim of the present paper.

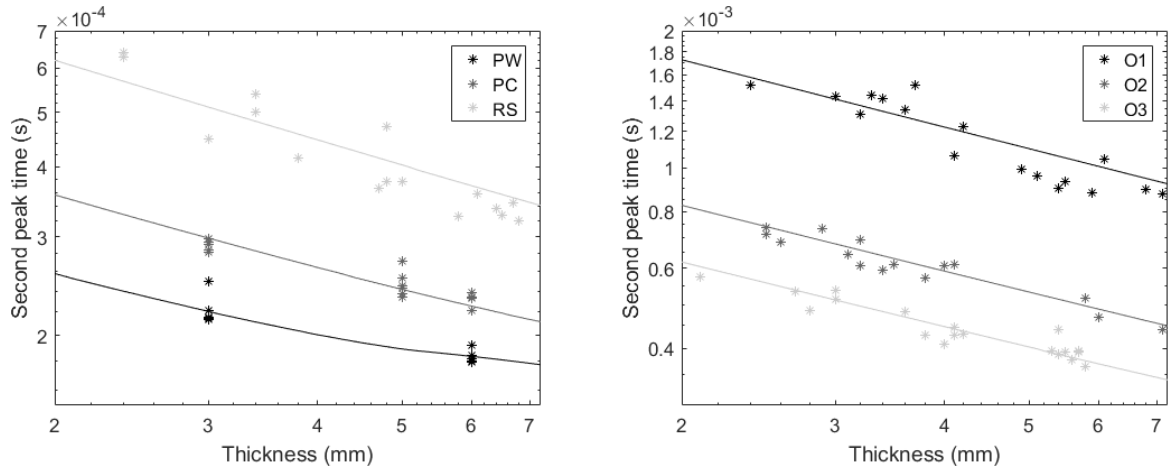

Figure 6. Comparison of the experimental and estimated values of the logarithm of the second peak time τ obtained for the different materials tested.

Material	ε_m (%)	ε^+ (%)	σ_ε (%)
PW	2	11	3
PC	4	11	3
RS	7	15	5
O1	7	17	5
O2	3	8	3
O3	4	12	4

Table 4: Thickness estimation performance. ε_m corresponds to the mean error between measured and estimated thickness, ε^+ is the maximum error obtained and σ_ε is the standard deviation on the error. All values are rounded upward and in percentage

Table 4 shows the average and maximum error obtained between the measured and estimated thickness using the optimized model. The maximum error obtained was 17% difference for one Orthobone 10PCF sample. In average, the relative error made on the thickness is lower than 10%.

4. Discussion

The originality of the present study was to introduce a new method to retrieve information on the mechanical and geometrical properties of the sample impacted during an osteotomy. An instrumented hammer recording the time variation of the force applied to the osteotome during the impact was employed in combination with a dedicated signal processing technique, in order to determine the thickness and stiffness of the material located around the osteotome tip.

4.1. Physical interpretation of the indicators

The mallet properties affects the results and constitute input data of the model. It is actually necessary to work with the same mallet in order to be able to pull the results together. However, the results do not depend on the force sensor as long as the sensor bandwidth includes all frequencies contained in the signal. The vise should also not affect the results as long as its rigidity is much larger than that of the system. In the future, it would be interesting to consider an accelerometer located in the osteotome, which should probably give similar results since measuring the acceleration is the same as measuring the force.

Simple physical interpretations can be made to understand the experimental and numerical results. During the initial stage of the impact, the hammer transmits mechanical energy to the osteotome, which induces a displacement of the osteotome toward the plate sample. The sample being fixed in a vise, it behaves as a damping system for the osteotome, which then bounces back toward the hammer, leading to a second contact and another exchange of energy between the two." was replaced with "During the first contact (around t_1=0.1 ms in Fig. 2), the hammer applies a force on the osteotome that is accelerated, and then bounces back on the material located at the other end of the osteotome (which is fixed in a vise and therefore behaves as a damping system for the osteotome). Therefore, the osteotome goes back in the direction of the hammer until the second contact (around t_2=0.3 ms in Fig. 2). Note that due to inertia effects (since m_h is much larger than m_o), the movement of the hammer is weakly affected by the first impact and therefore, the hammer continues its displacement in the direction of the sample. Between t_1 and t_2, since the contact is unilateral in B (the point located between the hammer and the osteotome), it is possible to have a rupture of the contact in B, which leads to a force vanishing during a certain duration, as shown in the example of Fig. 3. The phenomenon is reproduced after t_2, although a loss of contact does not always occur, until the hammer loses its momentum due to the repeated force pulses occurring at each contact. Therefore, the osteotome bounces back and forth between the hammer and the sample. As a consequence, we may consider a "vibration" of the osteotome between the sample and the hammer, which leads to an oscillation of the force applied between the osteotome and the hammer. In other words, the system considers two degrees of freedom given by the position of the osteotome and of the hammer, which allows to obtain oscillation such as the ones shown in Fig. 2. Note that the force did not go down to zero in all cases and that such event strongly depends on all parameters shown in Fig. 3. During the first impact, the osteotome is at rest while it is likely to move in the direction of the hammer during the second impact, depending on the parameters. Therefore, the amplitude of the second contact may be higher than that of the first impact in cases where the velocity of the hammer moving towards the sample is weakly modified during the first contact. This phenomenon iterates several times, until no more energy is exchanged. Three to five contacts generally occur during the impact within a few milliseconds. Each contact corresponds to a peak in the force signal (see Fig. 2). Note that similar results were obtained in [17] (see in particular Fig. 8 and 9 of [17]) in a different situation involving an acetabular cup implant and using finite element modeling.

The results obtained herein may be compared with [34], where a method to measure impact forces with small peak was proposed. However, the situation described in [34] was quite different because no hammer (or mass behind the impactor) was considered and the force was measured in a non-contact manner through optical means. The set-up described in [34] leads to a single peak of the force because the mechanical system was different in that it only has one degree of freedom, given by the position of the mass. This difference explains the fact that no oscillations comparable to those obtained herein were obtained in [34].

The results obtained herein may be compared with [35] where multiple peaks (with the force going down to zero in between the peaks) were obtained (see Fig. 3) when considering the impact of femoral stems in bone mimicking phantoms. Similarly, multiple peaks were also obtained in some situations corresponding to the impact of the acetabular cup inserted in anatomical subjects (see Fig. 5 of [18]) and *in vitro* (see Fig. 5 of [15]). However, in the aforementioned examples, the amplitude of the second peak was lower than that of the first peak, which may be explained by the different geometrical configuration.

Moreover, comparable results have been obtained in [17] using finite element analyses, as shown in Fig. 7a of [17]. Actually, the same physical interpretation as the one given above (i.e. the rebound of the ancillary between the hammer and the sample) had already been given in is fully illustrated in Fig. 8 that shows the different peaks as well as the oscillation of the ancillary (corresponding to the osteotome in the present study). Note that it is unlikely that possible vibrations of the hammer should not affect the signal obtained because the model described in Fig. 3 considers a rigid body motion for the hammer and is able to reproduce the experimental results.

4.1.1 Second peak time

The osteotome mechanical behavior is modeled as a damped system oscillating between the sample and the hammer. In the model described in subsection 2.2, the pulsation $\omega_o = (k_s/m_o)^{0.5}$ arises from Eqs 1 and 2. Since k_s is equal to $d\,w\,E/l$, the period of oscillation T_o is proportional to $(E\,d)^{-0.5}$. The second peak time τ is closely related to the period of oscillation T_o. In Fig. 6, $\log(\tau)$ is shown to depend linearly on $\log(d)$, with slope coefficients comprised between -0.38 and -0.49 for all materials, close to -0.5 coming from the expression of T_o given above. Similarly, the results shown in Fig. 4 (a) are in agreement with the aforementioned approximation of τ since the value of τ increases when the Young's modulus decreases. These results confirm that the second peak time is a relevant indicator to assess the dynamic behavior of the system.

4.1.2 Impulse ratio

The purpose of the impulse ratio λ is to provide complementary information on the material properties compared to using the second peak time τ only. The impulse ratio is the ratio of the energy exchanged during the second and first contacts, which is related to the material viscoelasticity. Figure 4 (b) shows that the values of λ decrease when the values $\tan\delta$ increase. Therefore, λ was used in combination with the second peak time τ to classify the different materials. Using a combination of both indicators allowed us to perform an efficient classification, with a prediction performance close to 90%.

4.2. Error and limitations of the method

4.2.1 Initial velocity of the hammer

When performing the measurements, we only focused at reaching a maximum force comprised between 150 N and 250 N without any other specific constraints on the impact realization. It would be interesting to investigate whether dropping the hammer or holding it in place during the impact would lead to any change on the signals.

The initial velocity v_h of the hammer defined in the analytical model was chosen constant and equal to 0.1 m/s, which constitutes an approximation. In the experimental protocol described in subsection 2.1, the maximum amplitude of the force F_o was comprised between 150 and 250 N. For a polycarbonate sample of the following characteristics: d = 3 mm, E = 1.6 GPa and $\tan\delta$ = 0.02, the velocity must be comprised between 0.077 m/s and 0.127 m/s to obtain F_o in the desired range, which justify the choice of v_h = 0.1 m/s. Note that the amplitude given by the model for v_h = 0.1 m/s is 195 N. Moreover, the value of v_h affects weakly the values of both the indicators τ and λ. Changing the value of v_h from 0.077 m/s to 0.127 m/s induces of variation in τ and λ lower than 0.2%, which validates the approximation of a constant value of v_h made in this study.

4.2.2 Viscoelasticity

Another source of error lies in the choice of a constant value for the mechanical loss $\tan\delta$, which is justified by the relatively weak sensitivity of the results to variations of $\tan\delta$. For example, for a 3 mm thick polycarbonate sample (E = 1.6 GPa and $\tan\delta = 2e^{-2}$), a change of ±20% in the value of E leads to a variation of around 8% of the value of τ and 2% of the value of λ. In contrast, the influence of $\tan\delta$ is much lower since a change of ±20% of the value of $\tan\delta$ leads to variation of around 0.1% of the value of τ and of around 0.3% of the value of λ. The low sensitivity of the parameters τ and λ to changes in $\tan\delta$ justifies why no estimation of $\tan\delta$ was carried out. However, including viscosity in the plate model is important and a purely elastic model instead of the Kelvin-Voigt model leads to analytical results quite different from the experimental results. Moreover, the choice of using values from the literature for $\tan\delta$ made in subsection 2.1, which constitutes a limitation of this study, is also justified by the low sensitivity of the results to variations of $\tan\delta$.

4.2.3 Other limitations

This study has several other limitations. First, crack propagation may occur when impacting the osteotome repeatedly with the hammer, which may in turn induce variations of the indicators τ and λ. In the experimental protocol described in subsection 2.1, the osteotome tip was brought to a depth of 2 mm into the material. This 2 mm penetration depth was chosen as a compromise between a sufficiently low value to avoid crack propagation and a sufficiently high value to obtain a stable positioning of the osteotome in the material. Similarly, compromises had to be found for the maximum amplitude of the force F_o which was bounded between 150 and 250 N. The upper bound was chosen to prevent crack propagation, while the lower bound was chosen to ensure that the data carried sufficient information on the material properties, while the 100 N range extent was considered wide enough to manually adjust the impact energy without having too much dispersion on the results. Note that the maximum amplitude of the force F_o could be

controlled easily in real time using the labview interface during impacts. It would be interesting to consider another contact geometry allowing to investigate crack propagation. To do so, we should provide impact with higher energy and monitor crack propagation using an adapted set-up such as for example video motion tracking. However, although investigating crack propagation is of interest, it is out of scope of the present paper and left for future studies.

Second, the 1-D model described in subsection 2.2 is very simple, and the Kelvin-Voigt model used for the plate samples does not accurately represent the behavior of all viscoelastic materials. It does not exhibit time-independent strain on loading or unloading, and does not describe a permanent strain after unloading either [25]. More advanced models may be used to derive more accurate estimation of the Young's modulus, at the expense of an increased complexity and computation time.

Third, another limitation lies in the choice of the different material types considered in this study. The performances of the classification depends on the differences in mechanical properties of the material types. Materials with too similar properties could lead to overlapping regions of interest in the dimensional space (τ, λ), which would make it impossible to derive an effective classification. Here, we choose to consider various inert materials in order to be able to work under standardized conditions. Although subject to an important variability, the Young's modulus of trabecular (respectively cortical) bone is typically around 50-500 Mpa (respectively 2-20 GPa) and the Young's modulus of cartilage is around 10-50 MPa. These orders of magnitude are in the range of the materials tested herein, even if the Young's modulus of cortical bone (respectively cartilage) is higher (respectively lower) than all materials considered. As a consequence, the method should be tested in the future with more rigid material in order to clearly determine whether cortical bone, that is more rigid than all materials considered herein, can also be tested using the method described herein. The extent to which the method can distinguish between strong and weak bones remains unknown.

Fourth, the Young's modulus identification (see subsection 2.3.2) was performed on a given data-set for which the thickness of each sample was known. In subsection 2.3.3, the thickness of each sample was determined using the optimized value of the Young's modulus, which was optimized on the same samples whose thickness are to be estimated. This can be regarded as a "training phase". Once the model is optimized, it can be used to predict the thickness of a new sample without any bias on the prediction. The implication here is that the present method cannot be used on a new set of material types without a learning phase first.

Fifth, the medium surrounding the tested material is likely to significantly affect the response of the system and this effect was not taken into account since all material were surrounded by air. In particular, the presence of soft tissue should induce an increase of τ (due to a lower resonance frequency) and of λ (due to a more important attenuation). However, the clinical situation is complex due to the presence of both air, liquid and soft tissues around bone and cartilage. Therefore, we choose to work in a standardized situation with air surrounding the material because it allows to obtain a situation that can easily be reproduced by others. Future experiments should be reproduced with various boundary conditions applied to the material.

Despite the aforementioned limitations and sources of errors, the approach developed herein allows to obtain an estimation of the material Young's modulus and the plate thickness with a sufficient precision to distinguish the different configurations. Since the aim is not to retrieve precise values of Young's modulus but rather to provide a distinction between cartilage, cortical and trabecular bone, further study should be carried out in this direction. Experimental measurements on cartilage and bone tissues are needed to train

the model on such materials. Moreover, the interoperator variability should be investigated in details in future study. In particular, the osteotome is held manually while applying a force. Different operators may hold the osteotome and the hammer differently and the effect of such variations should be quantified.

5. Conclusion and perspectives

Although the present method may be used for any kind of osteotomy, it is particularly interesting in the context of rhinoplasty because it could provide image-guided navigation and clinical decision support. When the surgeon defines the optimal path for the osteotome during the preoperative planning phase, the thickness of bone tissues along the path could be determined using preoperative CT images. Impact analysis could be used peroperatively to estimate bone thickness at the osteotome tip, to follow the correct progression of the osteotome, and to alert the surgeon if the osteotomy deviates from the planned trajectory. Moreover, information of the stiffness could help to evaluate the degree of bony fracture (greenstick or complete fractures), or anticipate adverse fractures as soon as they initiate and before they cause any disruption or collapsing of the nose.

Acknowledgements

This work has received funding from the European Research Council (ERC) under the European Union's Horizon 2020 research and innovation program (grant agreement No 682001, project ERC Consolidator Grant 2015 BoneImplant).

Bibliography

[1] R. B. Summers, “A new concept in maxillary implant surgery: the osteotome technique.” *Compendium (Newtown, Pa.)*, vol. 15, no. 2, pp. 152–154, 1994.

[2] N. Ferrigno, M. Laureti, and S. Fanali, “Dental implants placement in conjunction with osteotome sinus floor elevation: a 12-year life-table analysis from a prospective study on 588 iti R implants,” *Clinical oral implants research*, vol. 17, no. 2, pp. 194–205, 2006.

[3] M. F. Swiontkowski and S. D. Stovitz, *Manual of orthopaedics*, ch. Operating room equipment and techniques, p. 209. Lippincott Williams & Wilkins, 2012.

[4] F. J. Stucker, C. De Souza, G. S. Kenyon, T. S. Lian, W. Draf, and B. Schick, *Rhinology and facial plastic surgery*. Springer Science & Business Media, 2009.

[5] M. Z. Siemionow and M. Eisenmann-Klein, *Plastic and reconstructive surgery*, ch. Nasal Reconstruction and aesthetic rhinoplasty. Springer, 2010.

[6] R. K. Daniel, *Mastering rhinoplasty: a comprehensive atlas of surgical techniques with integrated video clips*. Springer Science & Business Media, 2010.

[7] A. Nijmeh, N. Goodger, D. Hawkes, P. Edwards, and M. McGurk, “Image-guided navigation in oral and maxillofacial surgery,” *British Journal of Oral and Maxillofacial Surgery*, vol. 43, no. 4, pp. 294–302, 2005.

[8] C. Schulz, S. Waldeck, and U. M. Mauer, “Intraoperative image guidance in neurosurgery: development, current indications, and future trends,” *Radiology research and practice*, vol. 2012, 2012.

[9] E. J. Dobratz and P. A. Hilger, “Osteotomies,” *Clinics in plastic surgery*, vol. 37, no. 2, pp. 301–311, 2010.

[10] M. A. Shiffman and A. Di Giuseppe, *Advanced aesthetic rhinoplasty: art, science, and new clinical techniques*. Springer Science & Business Media, 2013.

[11] J.-B. Duron, Y. Jallut, P. Nguyen, G. Aiach, and J. Bardot, “Osteotomies en rhino-´ plastie,” in *Annales de Chirurgie Plastique Esthetique´* , vol. 59, pp. 418–423, Elsevier, 2014.

[12] V. Mathieu, A. Michel, C.-H. F. Lachaniette, A. Poignard, P. Hernigou, J. Allain, and G. Haiat, “Variation of the impact duration during the in vitro insertion of acetabular cup implants,” *Medical Engineering and Physics*, vol. 35, no. 11, pp. 1558–1563, 2013.

[13] A. Michel, R. Bosc, V. Mathieu, P. Hernigou, and G. Haiat, “Monitoring the press-fit insertion of an acetabular cup by impact measurements: Influence of bone abrasion,” *Proceedings of the Institution of Mechanical Engineers, Part H: Journal of Engineering in Medicine*, vol. 228, no. 10, pp. 1027–1034, 2014.

[14] A. Michel, R. Bosc, R. Vayron, and G. Haiat, “In vitro evaluation of the acetabular cup primary stability by impact analysis,” *Journal of Biomechanical Engineering*, vol. 137, no. 3, p. 031011, 2015.

[15] A. Michel, R. Bosc, F. Sailhan, R. Vayron, and G. Haiat, “Ex vivo estimation of cementless acetabular cup stability using an impact hammer,” *Medical Engineering and Physics*, vol. 38, no. 2, pp. 80–86, 2016.

[16] V.-H. Nguyen, G. Rosi, S. Naili, A. Michel, M.-L. Raffa, R. Bosc, J.-P. Meningaud, C. Chappard, N. Takano, and G. Haiat, “Influence of anisotropic bone properties on the biomechanical behavior of the acetabular cup implant: a multiscale finite element study,” *Computer methods in biomechanics and biomedical engineering*, vol. 20, no. 12, pp. 1312–1325, 2017.

[17] A. Michel, V.-H. Nguyen, R. Bosc, R. Vayron, P. Hernigou, S. Naili, and G. Haiat, “Finite element model of the impaction of a press-fitted acetabular cup,” *Medical & biological engineering & computing*, vol. 55, no. 5, pp. 781–791, 2017.

[18] A. Michel, R. Bosc, J.-P. Meningaud, P. Hernigou, and G. Haiat, “Assessing the acetabular cup implant primary stability by impact analyses: a cadaveric study,” *PloS one*, vol. 11, no. 11, 2016.

[19] A. Tijou, G. Rosi, H. Albini Lomani, A. Dubory, C.-H. Flouzat-Lachaniette, and G. Haiat, “A cadaveric validation of a method based on impact analysis to monitor the femoral stem insertion,” *Journal of Journal of the Mechanical Behavior of Biomedical Materials*, Submitted.

[20] E. Garner, R. Lakes, T. Lee, C. Swan, and R. Brand, “Viscoelastic dissipation in compact bone: implications for stress-induced fluid flow in bone,” *Journal of biomechanical engineering*, vol. 122, no. 2, pp. 166–172, 2000.

[21] S. C. Cowin *et al.*, *Bone mechanics handbook*. CRC press, 2001.

[22] J. Othmezouri-Decerf, “Interpretation of the mechanical damping behaviour of glassy polycarbonate strained in the non-linear range of deformation below the yield point,” *Polymer*, vol. 29, no. 4, pp. 641–645, 1988.

[23] J. Heijboer, “Dynamic mechanical properties and impact strength,” in *Journal of Polymer Science: Polymer Symposia*, vol. 16, pp. 3755–3763, Wiley Online Library, 1967.

[24] L. Cremer and M. Heckl, *Structure-borne sound: structural vibrations and sound radiation at audio frequencies*, ch. Damping, pp. 149–235. Springer Science & Business Media, 2005.

[25] W. N. Findley and F. A. Davis, *Creep and relaxation of nonlinear viscoelastic materials*, ch. Linear viscoelastic constitutive equations, pp. 50–107. North-Holland, 2013.

[26] W. Kutta, “Beitrag zur naherungweisen integration totaler differentialgleichun-¨ gen,” *Zeit. Math. Physik*, vol. 46, 1901.

[27] J. C. Butcher, “Coefficients for the study of runge-kutta integration processes,” *Journal of the Australian Mathematical Society*, vol. 3, no. 2, pp. 185–201, 1963.

[28] J. C. Butcher, *Numerical methods for ordinary differential equations*. John Wiley & Sons, 2016.

[29] C. Cortes and V. Vapnik, "Support-vector networks," *Machine learning*, vol. 20, no. 3, pp. 273–297, 1995.

[30] V. Vapnik, *The nature of statistical learning theory*. Springer science & business media, 2013.

[31] T. G. Dietterich and G. Bakiri, "Solving multiclass learning problems via errorcorrecting output codes," *Journal of artificial intelligence research*, vol. 2, pp. 263–286, 1995.

[32] D. J. Wilde, "Optimum seeking methods," 1964.

[33] W. Sun and Y.-X. Yuan, *Optimization theory and methods*, vol. 1, ch. Line Search. Springer Science & Business Media, 2006.

[34] Fujii, Y. and J. Valera, *Impact force measurement using an inertial mass and a digitizer.* Meas. Sci. Technol, 2006. **17**: p. 863-868.

[35] Tijou, A., et al., *Monitoring cementless femoral stem insertion by impact analyses: An in vitro study.* J Mech Behav Biomed Mater, 2018. **88**: p. 102-108.

Figure Captions

Figure 1 - Schematic representation of the experimental set-up used for impaction of the osteotome on the samples. The sample is in the plane (*YZ)* and the plane of the osteotome is in the plane *(XZ)*.

Figure 2 – Signals corresponding to the variation of the force applied to the osteotome as a function of time obtained experimentally (solid line) and analytically (dashed line) for an impact realized on a 3 mm thick plywood sample. The first (respectively second and third) contact correspond to the first (respectively second and third) peak. The analytical signal corresponds to the solution given by Eqs. 1-2 ($m_h \ddot{x}_B$ is plotted) by considering: v_h= 0.1 m/s, E = 2400 MPa and tan δ = 0.01. The experimental signal correspond to one given impact and was not averaged.

Figure 3 – Schematic representation of the acoustical model used to account for the behavior of the damped oscillating system. A is the bilateral contact point between the osteotome and the sample. B is the unilateral contact point between the osteotome and the hammer. (a): Configuration where the hammer is in contact with the osteotome. (b): Configuration where the hammer is not in contact with the osteotome. The varying parameters of the model are k_s and η_s, which correspond to the stiffness and of the viscosity of the tested samples and which are function of the sample material.

Figure 4 – Distribution of the second peak time τ (a) and the impulse ratio λ (b) obtained experimentally for the different materials. *: not statistically different.

Figure 5 - Distribution of the values of τ and λ obtained for the 100 plate samples. Each material is indicated with a different marker, and the decision boundaries for material classification are indicated in solid lines.

Figure 6. Comparison of the experimental and estimated values of the logarithm of the second peak time τ obtained for the different materials tested.

Table Captions

Table 1: Mechanical properties of the six material types, and corresponding plates thickness distribution. E denotes the Young's modulus, $\tan\delta$ the mechanical loss, d_m the mean plate thickness, σ_d the standard deviation of the plate thickness, d^- the minimum plate thickness, d^+ the maximum plate thickness, and N the number of samples of each material. The reproducibility of the measurement of E is equal to around 10% for all samples.

Table 2: Parameters used in the acoustical model described in Fig. 3.

Table 3: Predicted apparent Young's moduli ($E_{predicted}$), Young's moduli measured using the tensile tests (E) and quality assessment of the model-based inversion given by RMSE, NRMSE and R.

Table 4: Thickness estimation performance. ε_m corresponds to the mean error between measured and estimated thickness, ε^+ is the maximum error obtained and σ_ε is the standard deviation on the error. All values are rounded upward and in percentage